

Traction Adaptive Motion Planning at the Limits of Handling

Lars Svensson*, Monimoy Bujarbaruah†, Arpit Karsolia‡, Christian Berger§, Martin Törngren*

September 10, 2020

Abstract

In this paper we address the problem of motion planning and control at the limits of handling, under locally varying traction conditions. We propose a novel solution method where locally varying traction is represented by time-varying tire force constraints. A constrained finite time optimal control problem is solved in a receding horizon fashion, imposing these time-varying constraints. Furthermore, we employ a sampling augmentation procedure to address the problems of infeasibility and sensitivity to local minima that arises when the constraint configuration is altered.

We validate the proposed algorithm on a Volvo FH16 heavy-duty vehicle, in a range of critical scenarios. Experimental results indicate that traction adaptation improves the vehicle's capacity to avoid accidents, both when adapting to low and high local traction.

1 Introduction

Automated driving and advanced driver assistance technology show increasing potential to improve safety and mobility of transportation systems in the future. A major challenge in driving automation is handling of critical situations, i.e., situations that appear suddenly, in which an accident is imminent. Critical situations may originate from multiple sources e.g., unpredictable behavior of other traffic agents or rapid changes in the operational conditions. The steady progress in sensors, perception and prediction algorithms indicate that a subset of critical situations can be anticipated and avoided ahead of time. However, considering the inherent unpredictability of humans in the traffic environment and the wide range of operational conditions, it is unlikely that all critical situations can be anticipated and avoided ahead of time, without sacrificing efficiency and availability by enforcing overly cautious behavior [1].

When a critical situation does occur, passenger comfort is no longer a priority, and if necessary, we wish to utilize the full physical capability of the vehicle to avoid the imminent accident. This motivates research in the field of motion planning and control at the limits of handling. Previous research efforts present methods for which performance approaches the physical limits [2, 3]. However, the motion capability of a road vehicle is greatly affected by locally varying traction conditions of the road. This phenomenon, that can be intuitively understood by the simple experiment depicted

*Division of Mechatronics and Embedded Control Systems, KTH Royal Institute of Technology, Stockholm, Swe.

†Model Predictive Control Laboratory at University of California Berkeley, USA.

‡Department of Electrical Engineering at Chalmers University of Technology, Sweden.

§Department of Computer Science and Engineering at University of Gothenburg, Sweden.



(a) Dry road surface



(b) Wet road surface

Figure 1: Example of how operational conditions dictate the dynamic capabilities of a road vehicle. Entering the curve at 15m/s, the vehicle comfortably negotiates the corner when the road is dry, but slides out into the opposing lane when the road is wet, causing a hazardous situation.

in Fig 1 has been well studied and is included in standard vehicle dynamics literature [4, 5], but has only recently been considered in the context of motion planning at the limits of handling [6].

The work presented in this paper represents a further step towards traction adaptive motion planning and control at the limits of handling. We propose a novel optimization based framework, in which the locally varying traction limit is represented as time-varying constraints on tire forces. The constraints are updated online as a function of the estimated friction coefficient and dynamic tire loads. Furthermore, we employ sampling augmentation to address the non-convexity and infeasibility issues of the arising optimization problem. We evaluate the proposed method in comparison with an equivalent non-adaptive scheme, in a sequence of experiments on various road surfaces.

The paper presents an extended and refined version of the method that was originally introduced in [7]. The extension includes refinement of the mathematical framework, a more accurate model of the vehicle and its traction limitations, a novel, GPU accelerated method to generate feasible sample trajectories, and an extensive experimental evaluation.

We summarize the contributions of the paper as follows:

1. A real-time capable algorithm for traction adaptive motion planning and control that produces optimal solutions with respect to time-varying tire force constraints.
2. An experimental evaluation of traction adaptive motion planning and control, showing that the concept improves capacity to avoid accidents in a range of critical scenarios, when adapting to low as well as high local traction.

2 Motivation

Critical scenarios at the limits of handling put the following high level requirements on the local motion planning functionality:

1. A relatively complex vehicle model is required to accurately describe the vehicle in aggressive motions.
2. A sufficiently long planning horizon is required to handle the inertia and limited actuation capacity of the vehicle.
3. A short planning time is required in order to react promptly to a dynamically changing traffic scene
4. The planner have to be able to make discrete decisions, e.g., to go left or right of an obstacle
5. Local traction variations should be considered.

Requirements 1) - 4) have been identified in previous academic works with state of the art approaches presented in Section 3. Next, we motivate why 5) should also be considered in this context.

From basic mechanics we have that for a single tire, the combined longitudinal, F_x , and lateral, F_y , force that can be exerted between tire and road is upper bounded by the friction coefficient μ times the normal force acting on the tire, F_z , i.e.,

$$\sqrt{F_x^2 + F_y^2} \leq \mu F_z. \quad (1)$$

This limit forms a circle in the lateral-longitudinal plane and is therefore commonly referred to as the friction circle¹.

Both μ and F_z typically vary substantially with time. The friction coefficient varies with e.g., road surface, tire temperature and wear, and the normal force varies as a result of road inclination and dynamic forces caused by vehicle motion. Fig. 2 highlights the impact of this phenomenon in terms of motion planning near the physical limits. The figure visualizes to what extent the force limits of the front and rear tires vary under different operational conditions and motion cases.

The phenomenon presents an additional challenge to motion planning in critical situations. For example, not considering it and assuming static bounds on tire forces will have one of two consequences when planning aggressive evasive maneuvers

1. **Planning of infeasible motions.** The real vehicle will be unable to track the plan.
2. **Reduced capability to avoid accident.** The planner will not be able to fully utilize the available traction to avoid an accident.

Both 1) and 2) reduce the vehicle's capacity to avoid accidents in critical situations. This conclusion motivates us to pursue the development of algorithms for motion planning and control at the limits of handling, with a time-varying traction boundary. Next, we give a brief summary of relevant academic works in related fields.

3 Related Work

Motion planning algorithms for automated vehicles can be roughly classified into random sampling based, graph search based, trajectory roll-out and optimization based [8,9]. Considering the special

¹The friction circle is an approximation of the true force boundary of a tire. In reality, different tires will have differently shaped force boundaries. Therefore, the framework presented in Section 5 is designed to allow any convex shape to represent the force limit. In this study however, we use a circular representation for simplicity.

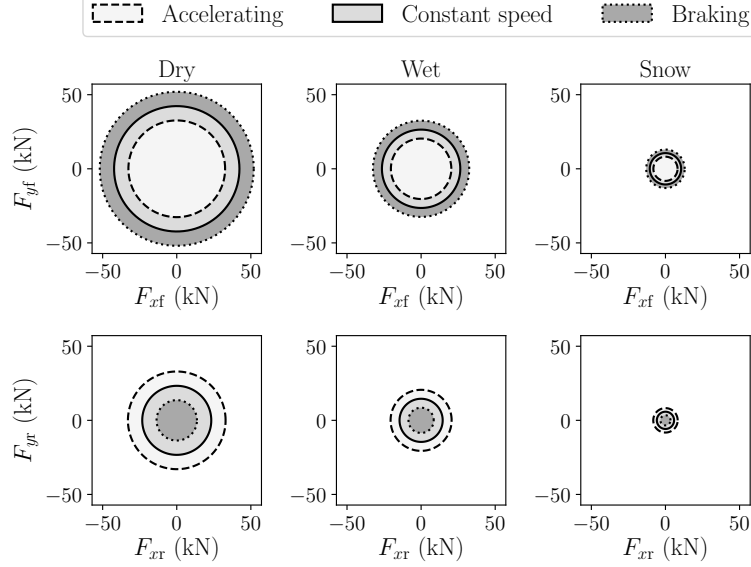


Figure 2: Numerical example of how tire force limits of our test vehicle vary at different operational conditions and motion cases, here represented by the following parameters: Dry: $\mu = 0.8$, Wet: $\mu = 0.5$, Snow: $\mu = 0.3$, Accelerating: $a_x = 0.5\text{m/s}^2$, Constant speed: $a_x = 0\text{m/s}^2$, Braking: $a_x = -0.5\text{m/s}^2$

requirements in critical scenarios stated in Section 2, there is an evident computational trade-off between properties 1), 2) and 3), and therefore, efficient solving of the motion planning problem is a key challenge. Previous studies, e.g., [2,3] show that optimization based methods are most well suited to handle such a computational trade-off. Furthermore, trajectory roll-out methods have been shown to be capable of handling requirement 4). Therefore, we delimit our related work section to these two categories of algorithms, as well as a few relevant concepts from the fields of friction estimation and adaptive control.

3.1 Optimization Based Methods

Optimization based methods dominate the field of motion planning at the limits of handling. Compared to other methods, they are not restricted to a discretized search space, scale comparatively well with model complexity [10], and allow explicit representation of constraints on states and inputs, which can be utilized to model physical limitations.

The basis of optimization based motion planning is to solve a Constrained Finite Time Optimal Control Problem (CFTOC) at each planning iteration, where the solution is the control and state sequence that obeys the constraints and minimizes a cost function over a fixed time horizon. In general, the CFTOC representing a collision avoidance motion planning problem is nonconvex, due to the nonlinear vehicle dynamics and nonconvex state constraints representing obstacles [11]. The nonconvexity of the problem renders the problem nontrivial to solve under the time requirements associated with critical evasive maneuvers. However, there exists several methods such as quasi-Newton algorithms with line search or Sequential Quadratic Programming (SQP) that are capable of solving the problem given a sufficiently near-optimal initial guess of the optimal trajectory [12–14]. SQP is an iterative approach in which a quadratic, and hence convex, approximation of the problem is formed and solved at each iteration. The approximation is obtained by performing a second order

approximation of the cost function and a linearization of dynamics and constraints at the solution from the previous iteration. Thus, a Quadratic Program (QP) is solved at each iteration. Diehl et al. proposed selecting the solution trajectory from the previous planning iteration as the initial guess, and perform a single SQP iteration per planning iteration [15–17]. This approach, called Real Time Iteration (RTI), is exceptionally computationally efficient and has been proven successful in numerous practical studies, including motion planning for automated vehicles [2, 10, 18, 19].

Ziegler et al. highlighted a drawback of the RTI approach in [10], noticing a sensitivity to local minima in situations where the motion planning problem contains discrete decision making. The intuition behind the phenomenon is that at each iteration the optimizer searches for the best solution locally around the initial guess, and therefore it is unlikely to find a solution in a different part of the state space, that may contain the globally optimal solution. Liniger et al. [2] identify the same issue and mitigate it by means of a high level path planner based on dynamic programming, a solution that works well in the particular application, but not for the general case.

3.2 Trajectory Roll-Out Methods

The trajectory roll-out concept represents a radically different approach to solving the motion planning problem. A large set of candidate trajectories are computed followed by a feasibility check and cost function evaluation that determines the optimal feasible candidate within the set [20–22]. Since the candidate trajectories are distributed across the drivable area, the method is less sensitive to local minima and thus performs well in situations where the motion planning problem contains discrete decisions.

Candidate trajectories are obtained by sampling either the control space, or the state space. Howard et al. showed that for highly constrained environments, such as road networks, state space sampling is more suitable [20] because it reduces the number of candidate trajectories that leave the drivable area. Computing the trajectory connecting the initial state to a single sampled goal state means solving a nonlinear optimal control problem, which is computationally intractable for large numbers of samples. However, for particular classes of trajectory candidates, e.g., quintic and quartic polynomials, these problems have closed form solutions [22]. While such a solution makes trajectory roll-out computationally tractable, the resulting reference trajectories are not suitable for maneuvers at the limits of handling, due to the inaccurate representation of vehicle dynamics and limitations.

3.3 Tire-Road Friction Estimation

There exists a large body of research on the topic of local estimation of the tire road friction coefficient from on-board vehicle measurements and knowledge of vehicle dynamics [23, 24]. Such estimates have previously been shown to improve performance in several vehicle control applications e.g., automatic emergency braking [25, 26] and path tracking control at deteriorated traction [27, 28]. With the recent developments in computer vision and machine learning, methods for predictive friction estimation using camera images have emerged [29–33]. A predictive friction estimate enables motion planning according to the traction conditions ahead of the vehicle.²

²A predictive estimate could also be obtained using a classical method such as, [23, 24], under the assumption that the traction conditions are unchanged for a short distance ahead of the vehicle.

3.4 Adaptive Control and Constraint Adaptation

To account for local variations in physical capabilities of the vehicle, we draw from developments in the field of adaptive control. Predictive control under model uncertainty has been a well-studied topic in recent literature [34–37]. Such frameworks allow the system to dynamically re-plan safer and more cost efficient trajectories with time, as model parameters get updated. We leverage this notion by utilizing updated model information to adapt the constraints of our optimization problem, to account for time-varying traction limitations.

3.5 Summary

To summarize, optimization based methods (RTI in particular) provides good performance in handling the trade-off between requirements 1), 2) and 3) in Section 2, but struggle with property 4). Trajectory roll-out methods on the other hand, inherently handle 4), but have much lower performance in the trade-off between 1), 2) and 3). The method proposed in this work combines RTI, trajectory roll-out and constraint adaptation to collectively address requirements 1) through 5). Furthermore, we designed the method to receive a predictive friction estimate from a state of the art method, but the estimation itself is not included in the scope of this paper.

4 Problem Formulation

In this section we introduce the mathematical details of the considered motion planning problem and state the challenges it presents in more detail.

4.1 Planning Model

Consider that the true dynamics of the vehicle are unknown, and that we receive closed-loop measurements of the vehicle state at regular time intervals of length T_s . For designing the planner/controller, we derive a continuous time model of the vehicle dynamics,

$$\dot{x}(t_c) = f_p(x(t_c), u(t_c)), \forall t_c \in [\bar{t}_c, \bar{t}_c + T_s), \quad (2)$$

with the state and input vectors

$$\begin{aligned} x &= [s, d, \Delta\psi, \dot{\psi}, v_x, v_y]^\top \in \mathbb{R}^n, \\ u &= [F_{yf}, F_{xf}, F_{xr}]^\top \in \mathbb{R}^m. \end{aligned}$$

Remark 1 We avoid separate notations for “nominal” states from (2) and the true states from the vehicle for the sake of notational simplicity in the remainder of the paper. This can be done as we do not opt for a robust control design approach, such as [38, 39].

State variables s , d and $\Delta\psi$ represent the progress along, the lateral deviation from and relative orientation to the lane center. Variables $\dot{\psi}$, v_x and v_y denote yaw angular velocity, longitudinal and lateral velocity of the vehicle. The input variables are the combined lateral force on the front tires, F_{yf} , the combined longitudinal force on the front tires, F_{xf} , and the combined longitudinal force on the rear tires F_{xr} . Furthermore, the model includes relations to determine the front and rear normal forces F_{zf} and F_{zr} from the state x_t , such that a time-varying traction force boundary can be obtained through (1). Further details on the model are provided in Appendix B.

For the discrete time controller synthesis in the following section, we discretize the planning model $f_p(\cdot, \cdot)$ in (2), and obtain a discrete time version denoted by $f(\cdot, \cdot)$ using one step forward Euler discretization as follows:

$$f(x_t, u_t) = x_t + T_s f_p(x(tT_s), u(tT_s)),$$

where $x_0 = x(0)$ and $u_t = u(tT_s)$ for all discrete time steps $t = \{0, 1, \dots\}$.

4.2 Optimal Control Problem

In optimization based motion planning, a Constrained Finite Time Optimal Control Problem (CFTOC) is solved at regular time intervals, producing a new motion plan at each planning iteration as its solution. For the motion planning problem with traction limit variation we consider the CFTOC

$$\begin{aligned} \min_{u_{0|t}, \dots, u_{N-1|t}} \quad & J(\mathcal{T}_t) \\ \text{s.t.,} \quad & x_{k+1|t} = f(x_{k|t}, u_{k|t}), \\ & u_{k|t} \in \mathcal{U}_{k|t}, \\ & x_{k|t} \in \mathcal{X}_{k|t}, \\ & \forall k \in \{0, 1, \dots, (N-1)\}, \\ & x_{0|t} = x_t, \quad x_{N|t} \in \mathcal{X}_{k|t}, \end{aligned} \tag{3}$$

where the variables $\{u_{0|t}, u_{1|t}, \dots, u_{N-1|t}\}$ denote a predicted input sequence at time step t , which, applied through the vehicle model $f(\cdot, \cdot)$ yields the corresponding predicted state sequence $\{x_{0|t}, x_{1|t}, \dots, x_{N|t}\}$. Note that since there are no closed-loop measurements available from the vehicle along the planning horizon in (3), $f_p(\cdot, \cdot)$ in (2) is propagated for $k \in \{0, 1, \dots, (N-1)\}$ to compute $f(\cdot, \cdot)$. The closed-loop state is reset again when x_{t+1} is measured.

We denote a predicted trajectory consisting of the associated predicted state and control sequences as

$$\mathcal{T}_t = \{\{x_{k|t}\}_{k=0}^N, \{u_{k|t}\}_{k=0}^{N-1}\},$$

which is used in the selected quadratic cost function

$$J(\mathcal{T}_t) = x_{N|t}^\top Q_N x_{N|t} + \sum_{k=0}^{N-1} (x_{k|t}^\top Q x_{k|t} + u_{k|t}^\top R u_{k|t}), \tag{4}$$

where $Q_N \succ 0$, $Q \succ 0$ and $R \succ 0$ are weight matrices that can be tuned by the designer. The choice here of a quadratic cost in (4) is done without loss of generality. Standard methods exist to make local quadratic approximations of non-quadratic cost functions, see Section 3.1.

In (3), the state trajectory constraints $\mathcal{X}_{k|t}$, for all $k \in \{0, 1, \dots, N\}$ represent collision free configurations of the vehicle with respect to the road geometry, static obstacles as well as positions and predicted positions of dynamic obstacles. Notice, the input constraints $\mathcal{U}_{k|t}$ are *time-varying* along the prediction horizon for $k \in \{0, 1, \dots, (N-1)\}$. This is the mechanism we use to model local traction limitations. The set $\mathcal{U}_{k|t}$ is computed at run-time as a function of the predicted friction estimate $\mu_{k|t}$ and normal forces F_{zf} and F_{zr} . A further description on how the tire force limits are obtained is described in Appendix B. Finally we let

$$\mathcal{T}_t^* = \{\{x_{k|t}^*\}_{k=0}^N, \{u_{k|t}^*\}_{k=0}^{N-1}\}$$

denote the optimal predicted trajectory.

4.3 Applying a State of the Art Approach: RTI

The Real Time Iteration approach [16, 40], RTI for short, is a state of the art approach for solving CFTOCs, that enables extraordinary computational efficiency [41]. In the context of motion planning in critical situations, computational efficiency is essential to achieve an acceptable trade-off between properties 1) 2) and 3) of Section 2. Hence, we select RTI as a starting point for algorithm development.

The central idea of the algorithm is to use the solution from the previous planning iteration to formulate a QP approximation of the CFTOC, which can be solved efficiently. The quadratic formulation is obtained by linearizing the dynamics and expressing the constraints as linear inequalities [11]. At a single planning iteration starting at time t , a standard RTI algorithm goes through the following steps:

First, the solution from the previous iteration \mathcal{T}_{t-1}^* is shifted one step forward in time, to compensate for the time passing between planning iterations. Thus, at time step t , an initial guess is obtained as,

$$\hat{\mathcal{T}}_t = \{\{\hat{x}_{k|t}\}_{k=0}^N, \{\hat{u}_{k|t}\}_{k=0}^{N-1}\},$$

where $\hat{x}_{k|t} = x_{k+1|t-1}^*$ and $\hat{u}_{k|t} = u_{k+1|t-1}^*$ for $k \in \{1, 2, \dots, (N-1)\}$ ³. Next, the dynamics are linearized about $\hat{\mathcal{T}}_t$. The system model matrices are obtained as

$$A_{k|t} = \left. \frac{\partial f}{\partial x} \right|_{(\hat{x}_{k|t}, \hat{u}_{k|t})}, \quad B_{k|t} = \left. \frac{\partial f}{\partial u} \right|_{(\hat{x}_{k|t}, \hat{u}_{k|t})},$$

for all $k \in \{0, 1, \dots, (N-1)\}$. State and input constraints are expressed as sets of linear inequalities:

$$\begin{aligned} \mathcal{P}_{k|t}^{\mathcal{X}} &= \{x : H_{k|t}^{\mathcal{X}} x \leq h_{k|t}^{\mathcal{X}}\} \subseteq \mathcal{X}_{k|t}, \\ \mathcal{P}_{k|t}^{\mathcal{U}} &= \{u : H_{k|t}^{\mathcal{U}} u \leq h_{k|t}^{\mathcal{U}}\} \subseteq \mathcal{U}_{k|t}, \end{aligned}$$

with $H_{k|t}^{\mathcal{X}} \in \mathbb{R}^{s_x \times n}$, $h_{k|t}^{\mathcal{X}} \in \mathbb{R}^{s_x}$, for all $k \in \{0, 1, \dots, N\}$, and $H_{k|t}^{\mathcal{U}} \in \mathbb{R}^{s_u \times m}$, $h_{k|t}^{\mathcal{U}} \in \mathbb{R}^{s_u}$ for all $k \in \{0, 1, \dots, (N-1)\}$. The procedure we use to linearize the input constraints of our vehicle model is described in Appendix B.

The final RTI style reformulation of (3) around an initial guess $\hat{\mathcal{T}}_t$ is shown in (5).

$$\begin{aligned} V^*(x_t, \hat{\mathcal{T}}_t) &:= \\ \min_{\Delta u_{0|t}, \dots, \Delta u_{N-1|t}} & \quad J(\mathcal{T}_t), \text{ with } \mathcal{T}_t = \{\{x_{k|t}\}_{k=0}^N, \{u_{k|t}\}_{k=0}^{N-1}\}, \\ \text{s.t.,} & \quad x_{k+1|t} = A_{k|t}(\Delta x_{k|t}) + B_{k|t}(\Delta u_{k|t}) + \hat{x}_{k+1|t}^*, \\ & \quad (\text{linearized about } \hat{\mathcal{T}}_t) \\ & \quad u_{k|t} \in \mathcal{P}_{k|t}^{\mathcal{U}}, \\ & \quad \forall k \in \{0, 1, \dots, (N-1)\}, \text{ with} \\ & \quad [\Delta x_{k|t}, \Delta u_{k|t}] = [x_{k|t} - \hat{x}'_{k|t}, u_{k|t} - \hat{u}'_{k|t}], \\ & \quad x_{k|t} \in \mathcal{P}_{k|t}^{\mathcal{X}}, \\ & \quad \forall k \in \{0, 1, \dots, N\}, \\ & \quad x_{0|t} = x_t, \end{aligned} \tag{5}$$

³Forward shifting is not possible for the N -th predicted state. So the final control input is duplicated $\hat{u}_{N-1|t} = u_{N-1|t-1}^*$ and the final state is obtained by integrating the dynamics forward $\hat{x}_{N|t} = f(x_{N-1|t-1}^*, u_{N-1|t-1}^*)$.

When a solution of (5) for time step t is obtained, the control

$$u_t = u_{0|t}^*,$$

is applied to the vehicle system through the low level control interface described in Appendix C. At the next time step, $(t + 1)$, problem (5) is solved again.

4.4 Challenges in Solving the RTI Problem (5)

The RTI algorithm builds on the assumption that \mathcal{T}_{t-1}^* is a feasible and near-optimal initial guess for time step t . If this is not the case, performance of the algorithm deteriorates, leading to three essential drawbacks with respect to the problem formulation of this paper.

- (i) *Infeasibility w.r.t. $\mathcal{P}_{k|t}^{\mathcal{U}}$* : In the presence of time-varying input constraints, there is no guarantee that at time step t the input sequence from, \mathcal{T}_{t-1}^* is feasible with respect to $\mathcal{P}_{k|t}^{\mathcal{U}}$, i.e., the condition $u_{k|t-1}^* \in \mathcal{P}_{k|t}^{\mathcal{U}}$ may or may not hold for all $k \in \{1, 2, \dots, N\}$.
- (ii) *Infeasibility w.r.t. $\mathcal{P}_{k|t}^{\mathcal{X}}$* : Irrespective of (i), in a dynamically changing environment with sensor limitations and unpredictable moving human actors, there is no guarantee that at time step t , the state sequence of \mathcal{T}_{t-1}^* will be collision free, i.e., the condition $x_{k|t-1}^* \in \mathcal{P}_{k|t}^{\mathcal{X}}$ may or may not hold for all $k \in \{1, 2, \dots, N\}$.
- (iii) *Sensitivity to local minima*: Because the search for \mathcal{T}_t^* is only performed locally around \mathcal{T}_{t-1}^* , RTI is prone to suboptimal decision making where the planning problem includes discrete decision making. In any traffic scene, new discrete decisions may appear dynamically [10].

Problem (i) is unique to our problem formulation, and stems from the addition of traction adaptation through time-varying input constraints $\mathcal{P}_{k|t}^{\mathcal{U}}$ introduced in (3). A naive solution is to project $u_{k|t-1}^*$ onto $\mathcal{P}_{k|t}^{\mathcal{U}}$ for all $k \in \{1, 2, \dots, (N - 1)\}$ and recompute $\hat{\mathcal{T}}_t$ from the dynamics model (this is the first step of our proposed algorithm, see Section 5.1). However, this is not a complete solution as it merely transforms problem (i) into problem (ii). Problem (ii) has been identified in previous works and is unavoidable in a dynamic traffic environment. Computational feasibility can be obtained by introducing slack variables, such that state constraint violations are allowed, but with a very high cost [2, 42]. Commonly however, this approach merely transforms Problem (ii) into Problem (iii). Problem (iii) in turn may be handled for specific applications by a higher level decision making layer [2]. In critical situations however, the optimal decision (e.g. to swerve left or right of a suddenly appearing obstacle) is highly dependent on e.g., the geometry of the traffic scene, the vehicle's state, dynamics and dynamic limitations. This information is typically only available at the local motion planning level and therefore, an informed decision can only be made there. In such critical decision making, insufficient scene understanding may lead to suboptimal decisions regarding the selected maneuvers, which in turn reduces capacity to avoid accidents. Trajectory roll-out methods, in contrast to optimization based methods, inherently handle such decisions by construction at the local planning level, as described in Section 3.2.

In the next section, we present a novel variant of RTI, which we refer to as Sampling Augmented Adaptive RTI (SAA-RTI), to jointly address (i), (ii) and (iii).

5 Sampling Augmented Adaptive RTI

The SAA-RTI algorithm decomposes the solving of (3) into four steps using the same planning horizon N and time discretization step T_s . Furthermore, steps C and D use the same cost function (4). The steps are:

- A. Ensuring input feasibility of \mathcal{T}_{t-1}^* ,
- B. Generating additional initial guess candidates through sampling,
- C. Selection of initial guess trajectory
- D. Constraint adaptive trajectory optimization.

Together, the above steps A-D remedy the limitations (i), (ii) and (iii) of RTI introduced in Section 4.4. In the following sub-sections we elaborate the details of each of the steps.

5.1 Ensuring Input Feasibility of \mathcal{T}_{t-1}^*

Due to the time-varying input constraints, situations when $u_{k|t-1}^* \notin \mathcal{P}_{k|t}^{\mathcal{U}}$ for $k \in \{1, 2, \dots, (N-1)\}$ may occur. To resolve this, we replace the shifting procedure in conventional RTI as:

$$\tilde{u}_{k|t} = \text{Proj}_{\mathcal{P}_{k|t}^{\mathcal{U}}}(u_{k+1|t-1}^*), \quad \forall k \in \{0, 1, \dots, (N-1)\}, \quad (6)$$

where $\text{Proj}_{\Omega}(\cdot)$ denotes Euclidean projection operation to the set Ω . Thus, we modify individual inputs if needed, such that $\tilde{u}_{k|t} \in \mathcal{P}_{k|t}^{\mathcal{U}}$ for $k \in \{0, 1, \dots, (N-1)\}$. Then, under the new input sequence, we propagate the system forward from $\tilde{x}_{0|t} = x_{1|t-1}^*$ to determine the state sequence $\tilde{x}_{k+1|t} = f(\tilde{x}_{k|t}, \tilde{u}_{k|t})$, $k \in \{1, 2, \dots, (N-1)\}$. Thereby, we obtain an initial guess

$$\tilde{\mathcal{T}}_t = \{\{\tilde{x}_{k|t}\}_{k=0}^N, \{\tilde{u}_{k|t}\}_{k=0}^{N-1}\}, \quad (7)$$

that satisfies dynamics and time-varying input constraints, resolving limitation (i) of Section 4.

We acknowledge that the procedure may alter the state sequence such that state constraints are violated, i.e., $\tilde{x}_{k|t} \notin \mathcal{P}_{k|t}^{\mathcal{X}}$, for some $k \in \{0, 1, \dots, N\}$. However, as stated in Problem (ii) in Section 4.4, this problem has to be addressed regardless of this addition, due to the dynamic environment. We address the problem in the next step of the algorithm by employing the trajectory roll-out concept [20].

5.2 Generating Additional Initial Guess Candidates Through Sampling

To handle the case when the initial guess (7) violates the state constraints, $\tilde{x}_{k|t} \notin \mathcal{P}_{k|t}^{\mathcal{X}}$ for any $k \in \{1, 2, \dots, N\}$ (i.e., Problem (ii)), and to avoid highly suboptimal local minima (i.e., Problem (iii)), we employ a further developed version of the sampling augmentation concept that was first introduced in [7].

The procedure starts by selecting N_s reference states $x_{\text{ref}}^{(i)}$, $i \in \{1, 2, \dots, N_s\}$ uniformly distributed within the lane ahead of the vehicle, and in the range of admissible velocities. For each reference state, we integrate the dynamics forward,

$$\hat{x}_{k+1|t}^{(i)} = f(\hat{x}_{k|t}^{(i)}, \hat{u}_{k|t}^{(i)}), \quad \forall k \in \{0, 1, \dots, (N-1)\}, \quad (8)$$

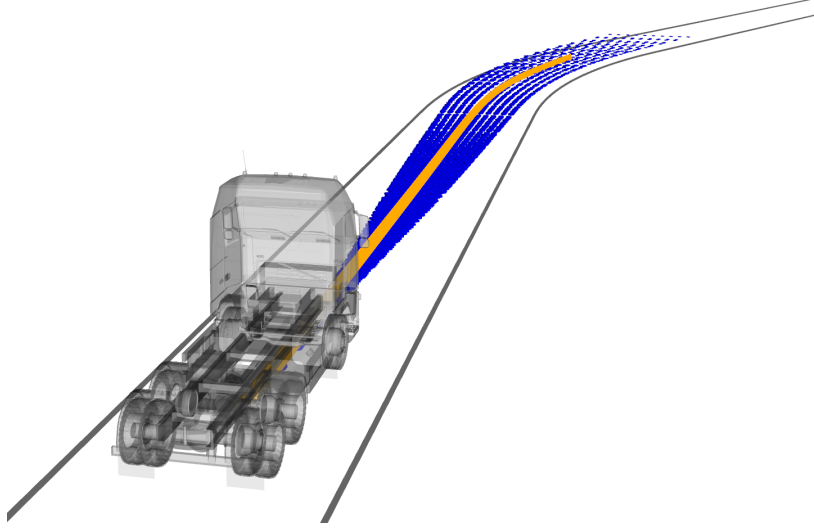


Figure 3: Visualization snapshot from single planning iteration showing the complete trajectory set $\hat{\mathcal{S}}_t \cup \tilde{\mathcal{T}}_t$ (blue) (in this case of 226 trajectories in total) and the selected initial guess $\hat{\mathcal{T}}'_t$ (orange).

from the initial state $\hat{x}_{0|t}^{(i)} = x_t$, towards the reference state under a Linear Quadratic Tracking (LQT) controller, for all $i \in \{1, 2, \dots, N_s\}$. At each time step k , the optimal control input is computed as

$$\hat{u}_{k|t}^{(i)} = -K_t(\hat{x}_{k|t}^{(i)} - x_{\text{ref}}^{(i)}), \quad (9)$$

where K_t is the optimal gain matrix, recomputed at each planning iteration by linearizing the dynamics around the the initial state x_t and solving the Discrete-time Algebraic Riccati Equation. To ensure $\hat{u}_{k|t}^{(i)} \in \mathcal{P}_{k|t}^{\mathcal{U}}$ for $k \in \{1, 2, \dots, N\}$ we apply the procedure described in Section 5.1 to project all control inputs onto the feasible set before propagating the state. The N_s candidate trajectories

$$\hat{\mathcal{T}}_t^{(i)} = \{\{\hat{x}_{k|t}^{(i)}\}_{k=0}^N, \{\hat{u}_{k|t}^{(i)}\}_{k=0}^{N-1}\},$$

for all $i \in \{1, 2, \dots, N_s\}$ are stored in the trajectory set

$$\hat{\mathcal{S}}_t = \bigcup_{i=1}^{N_s} \hat{\mathcal{T}}_t^{(i)}. \quad (10)$$

Notice that following the computation of K_t , each trajectory is computed independently, enabling efficient GPU acceleration.

5.3 Selection of Initial Guess Trajectory

To determine the best available initial guess, each candidate trajectory in the set $\hat{\mathcal{S}}_t \cup \tilde{\mathcal{T}}_t$ is evaluated based on the shared cost function $J(\cdot)$ in (4). The lowest cost candidate, i.e.,

$$\hat{\mathcal{T}}'_t = \arg \min_{\hat{\mathcal{T}}_t \in \hat{\mathcal{S}}_t \cup \tilde{\mathcal{T}}_t} (J(\hat{\mathcal{T}}_t)) \quad (11)$$

is selected for subsequent optimization. Trajectory candidates that violate state constraints, i.e., $\hat{x}_{k|t} \notin \mathcal{P}_{k|t}^{\mathcal{X}}$ for any $k \in \{1, 2, \dots, N\}$ are disregarded in the selection. Figure 3 shows a snapshot of $\hat{\mathcal{S}}_t \cup \tilde{\mathcal{T}}_t$ and $\hat{\mathcal{T}}'_t$ from a single planning iteration.

In case $\tilde{\mathcal{T}}_t$ is colliding or is in a highly suboptimal local minima, an alternative feasible and near-optimal initial guess can be obtained from $\hat{\mathcal{S}}_t$. Thus, we exploit the inherent redundancy in the trajectory roll-out concept [22], to resolve Problems (ii) and (iii) of Section 4. This property of the algorithm is experimentally verified in Section 6.4.

Remark 2 *In cases when changes to the time-varying state and input constraints are small between planning iterations, it is highly probable that $\hat{\mathcal{T}}'_t = \tilde{\mathcal{T}}_t$. In this case, algorithm behavior is identical to that of RTI. This is further elaborated in Section 6.4.*

5.4 Constraint Adaptive Trajectory Optimization

With the initial guess $\hat{\mathcal{T}}'_t$ obtained from (11), the final step of the SAA-RTI algorithm is to solve the QP

$$\begin{aligned}
V^*(x_t, \hat{\mathcal{T}}'_t) := & \min_{\Delta u_{0|t}, \dots, \Delta u_{N-1|t}} J(\mathcal{T}_t), \text{ with } \mathcal{T}_t = \{\{x_{k|t}\}_{k=0}^N, \{u_{k|t}\}_{k=0}^{N-1}\}, \\
& \text{s.t.,} \quad x_{k+1|t} = A_{k|t}(\Delta x_{k|t}) + B_{k|t}(\Delta u_{k|t}) + \hat{x}'_{k+1|t}, \\
& \quad \text{(linearized about } \hat{\mathcal{T}}'_t), \\
& \quad u_{k|t} \in \mathcal{P}_{k|t}^{\mathcal{U}}, \\
& \quad \forall k \in \{0, 1, \dots, (N-1)\}, \text{ with} \\
& \quad [\Delta x_{k|t}, \Delta u_{k|t}] = [x_{k|t} - \hat{x}'_{k|t}, u_{k|t} - \hat{u}'_{k|t}], \\
& \quad x_{k|t} \in \mathcal{P}_{k|t}^{\mathcal{X}}, \\
& \quad \forall k \in \{0, 1, \dots, N\}, \\
& \quad x_{0|t} = x_t.
\end{aligned} \tag{12}$$

Contrary to (5), the QP is initialized at $\hat{\mathcal{T}}'_t$, i.e., with the system model matrices given as

$$A_{k|t} = \left. \frac{\partial f}{\partial x} \right|_{(\hat{x}'_{k|t}, \hat{u}'_{k|t})}, \quad B_{k|t} = \left. \frac{\partial f}{\partial u} \right|_{(\hat{x}'_{k|t}, \hat{u}'_{k|t})},$$

for all $k \in \{0, 1, \dots, (N-1)\}$. After solving (12) at any time step t , we apply the closed-loop command

$$u_t = u_{0|t}^* \tag{13}$$

to the vehicle system through the low level control interface described in Appendix C. At $(t+1)$, (12) is re-solved.

5.5 Summary

We summarize SAA-RTI in Algorithm 1. Here, M_t represents local map features, e.g., lane boundaries and static obstacles, and O_t denotes dynamic obstacles at time step t . Also, at any time step t , we assume tire-road friction estimates $\mu_{k|t}$ for $k \in \{0, 1, \dots, (N-1)\}$ are obtained.

Algorithm 1 The SAA-RTI Algorithm

```
1: Initialization:  $\mathcal{T}_{t-1}^* = \emptyset$ 
2: while  $t \geq 0$  do
3:   Inputs:  $x_t, \mathcal{T}_{t-1}^*, M_t, O_t, \mu_{k|t}, \forall k \in \{0, 1, \dots, N\}$ 
4:   if  $\mathcal{T}_{t-1}^* \neq \emptyset$  then
5:      $\tilde{\mathcal{T}}_t \leftarrow \text{ShiftAndEnsureFeasibility}(\mathcal{T}_{t-1}^*, \mu_{k|t}, \forall k)$ 
6:   else
7:      $\tilde{\mathcal{T}}_t = \emptyset$ 
8:   end if
9:    $\hat{\mathcal{S}}_t \leftarrow \text{FeasibleTrajRollout}(x_t, M_t, \mu_{k|t}, \forall k)$  from (10)
10:   $\hat{\mathcal{T}}'_t = \arg \min_{\hat{\mathcal{T}}_t \in \hat{\mathcal{S}}_t \cup \tilde{\mathcal{T}}_t} (J(\hat{\mathcal{T}}_t))$  from (11)
11:   $A_{k|t}, B_{k|t} \leftarrow \text{LinearizeModel}(\hat{\mathcal{T}}'_t, \forall k)$ 
12:   $\mathcal{P}_{k|t}^{\mathcal{U}} \leftarrow \text{InputConstraints}(\hat{\mathcal{T}}'_t, \mu_{k|t}, \forall k)$ 
13:   $\mathcal{P}_{k|t}^{\mathcal{X}} \leftarrow \text{StateConstraints}(\hat{\mathcal{T}}'_t, O_t, M_t, \forall k)$ 
14:   $\mathcal{T}_t^* = \{\{x_{k|t}^*\}_{k=0}^N, \{u_{k|t}^*\}_{k=0}^{N-1}\} \leftarrow \text{Solve}$  (12)
15:  Apply  $u_{t|t}^*$  to the vehicle
16: end while
```

6 Experimental Evaluation

We evaluate the performance of Algorithm 1 (abbreviated TA), in terms of its capacity to avoid accidents in critical scenarios. We compare the algorithm with a baseline non-adaptive RTI scheme with static tire force constraints (abbreviated NA). The TA scheme uses time-varying tire force constraints computed as a function of predicted normal forces and a predictive tire-road friction estimate $\mu_{k|t} = \mu_{\text{est}}(s)$ for all $k \in \{0, 1, \dots, (N-1)\}$ as per equations (16) and (17) in Appendix B with traction utilization factor $\lambda = 0.90$ for all scenarios. Whereas the NA scheme uses static tire force constraints associated with a static friction estimate $\mu_{k|t} = \mu_{\text{sta}}$ for all $k \in \{0, 1, \dots, (N-1)\}$ and $a_x = 0$.

The critical scenarios selected for evaluation are:

- (i) *Turn at Low Local Traction*
- (ii) *Collision Avoidance at Low Local Traction*
- (iii) *Collision Avoidance at High Local Traction*
- (iv) *Collision Avoidance with Discrete Decisions*

Scenarios (i), (ii) and (iii) are designed to test the traction adaptive aspect, whereas Scenario (iv) is designed to evaluate the sampling augmentation aspect of the algorithm.

For the evaluation in this paper, we assume that an accurate predictive friction estimate is available, i.e., $\mu_{\text{est}}(s) = \mu_{\text{gt}}(s)$, where $\mu_{\text{gt}}(s)$ denotes the ground truth tire-road friction, which was obtained for the experiments by performing friction measurements ahead of time and storing the values in a map of the track. The tests were performed on completely flat road surfaces and therefore, evaluation of the effects of road inclination is not included in this work, i.e., $\theta = \phi = 0$ rad. in (14), Appendix B. In the collision avoidance scenarios, all suddenly appearing obstacles remain at a static position after appearing.

Remark 3 *This delimitation in the evaluation is not done because of limitations in the evaluated algorithms with respect to dynamic obstacles. For both the TA and NA schemes, state constraints $\mathcal{P}_{k|t}^{\mathcal{X}}$ are set individually for each $k \in \{0, 1, \dots, N\}$. Hence, including avoidance of e.g., a confidence interval of predicted positions of the obstacle is trivial from the planning perspective. Rather, the delimitation was made to ensure consistency between runs, and to avoid introducing additional uncertainty from the prediction functionality. Since the traction adaptive and the non-adaptive schemes are equivalent in this regard, we are confident that the conclusions we make for static obstacles will also hold for dynamic obstacles.*

In the following sub-sections, 6.1, 6.2, 6.3 and 6.4, we present and discuss results from each of the scenarios. The experimental setup is detailed in Appendix A.

6.1 Scenario (i): Turn at Low Local Traction

At the start of the first critical scenario at $t_c = 0$ s and $s = 0$ m, the vehicle approaches a turn at 8 m/s. Traction has deteriorated such that $\mu_{\text{gt}}(s) = 0.2$ for $s \geq 0$ m instead of the previous $\mu_{\text{gt}}(s) = 0.8$ for $s < 0$ m. The objective of the vehicle is to maintain its initial velocity and stay close to the center of the lane. Fig. 4, shows a driving behavior analysis comparing the TA scheme with time-varying tire force constraints corresponding to $\mu_{\text{est}}(s) = \mu_{\text{gt}}(s)$ and the NA scheme with static tire force constraints corresponding to $\mu_{\text{sta}} = 0.8$.

Not Adapting to Low Local Traction

We make the following observations of the behavior under the NA scheme. At $t_c = 0$ s, before reaching the corner, Fig. 4a, the planned motion appears to follow the intended objective of tracking the center of the lane and maintaining velocity. Immediately after entering the corner, Fig. 4c, the vehicle starts to exhibit under-steering behavior that was not previously anticipated (i.e., the planned motion at $t_c = 0$ s did not include this motion), and the plan gets gradually shifted towards the outside of the corner. The vehicle continues to under-steer heavily, (see front slip angle in Fig. 4l), soon entering the opposing lane, Fig. 4e, at a velocity of 7m/s Fig. 4k. At this point in the experiment, the planner disengages and full brake is applied. The vehicle eventually comes to a stop 15m outside of the lane, Fig. 4g. The planned trajectory at the beginning of the scenario, Fig. 4a, differs dramatically from the resulting closed loop trajectory, Figs. 4c, 4e, 4g.

The reason behind this undesirable behavior is evident from the planned tire forces at $t_c = 0$ s, plotted in Fig. 4i. The dashed blue and dotted orange lines represent the maximum horizontal forces that can be generated by the front and rear tires respectively, according to (1), given the recorded state trajectory. It is clear that the non-adaptive scheme plans tire forces (solid blue) that violate the physical limitations. Therefore, the vehicle is unable to realize the planned motion and promptly veers out of its lane.

Adapting to Low Local Traction

The adaptive scheme however, sets the tire force constraints dynamically according to the predictive friction estimate $\mu_{\text{est}}(s)$. Therefore the planned tire forces (dash-dotted orange in Fig. 4i) do not violate the physical limitations of the tires. Instead, it plans a motion, Fig. 4b, that minimizes the deviation from the objective (track the center of the lane and maintain 8 m/s), while satisfying the updated tire force constraints. With the TA scheme, the vehicle slows down from 8m/s to 5.5m/s before entering the corner, Fig. 4k and keeps a position on the outside of the turn. About a third of the way through the turn, Fig. 4d, the vehicle has cut across the lane and is positioned along

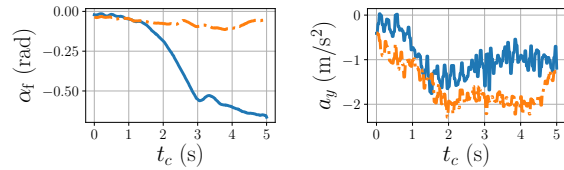
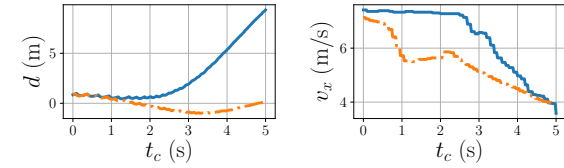
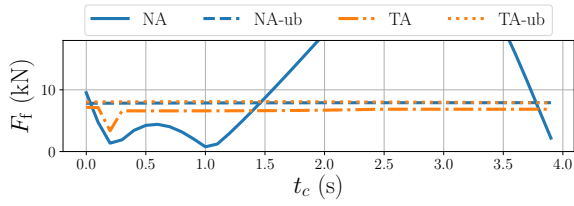
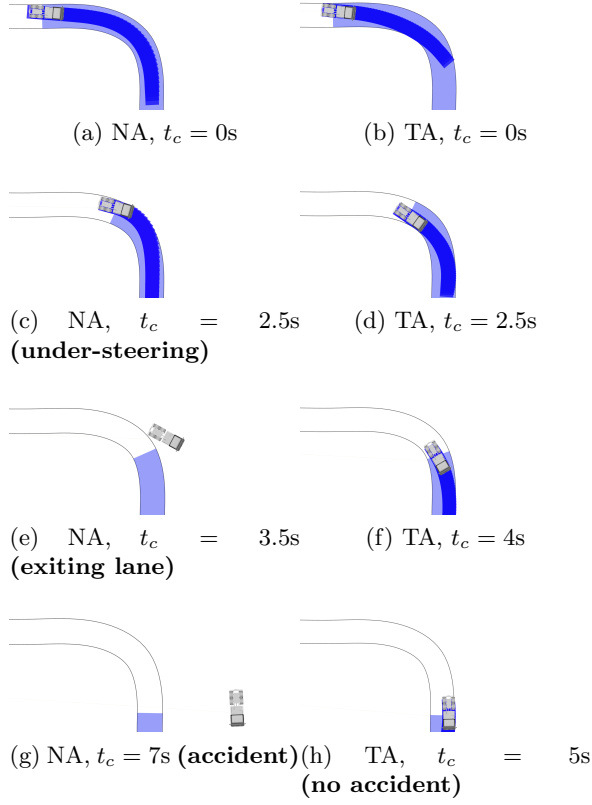


Figure 4: Scenario (i), turn at low μ . Sub-figures 4a through 4h show overhead visualizations of the planned motion. The left and right columns correspond to the non-adaptive (NA) and traction adaptive (TA) schemes respectively. Subfigure 4i show planned tire forces and prevailing force limits for the front and rear tires at $t_c = 0\text{s}$. Sub-figures 4j, 4k, 4l and 4m show comparisons in terms of deviation from the lane center, velocity, front wheel slip angle and lateral acceleration.

the inside of the corner, Fig. 4j. Towards the end of the turn, Fig. 4h, it starts cutting back across to the outside of the corner. Finally, the vehicle completes the turn safely, positioned at the outer edge of the lane, Fig. 4h, Fig. 4j. In contrast to the NA scheme, here the planned trajectory at the beginning of the scenario, Fig. 4b, corresponds well with the closed loop trajectory of the vehicle, Figs. 4d, 4f, 4h,

We break this behavior down into three coordinated characteristics of the maneuver that enable the vehicle to successfully negotiate the turn. First, contrary to the NA scheme, the TA scheme generates feasible tire force commands, utilizing approximately 90% ($\lambda = 0.90$) of the available traction for this surface, see Fig. 4i. This in turn generates slip angles within acceptable limits, Fig 4l, yielding high lateral acceleration, Fig 4m. Second, the maneuver utilizes the full width of the lane to minimize the curvature of the vehicle trace, thus reducing the lateral acceleration required to negotiate the turn. Third, the longitudinal velocity is reduced early in the maneuver such that the maximum tire forces are sufficient to negotiate the turn.

These coordinated adjustments to the motion plan are a direct result of the reduced tire force constraint set $\mathcal{P}_{k|t}^{\mathcal{U}}$, for all $k \in \{0, 1, \dots, (N-1)\}$ in the optimization problem (12). The planned motion utilizes 90% of the available local traction, such that control authority is maintained throughout the maneuver. Thus, the planning/control scheme safely mitigates the critical situation. Next, we evaluate the traction adaptation concept in collision avoidance scenarios.

6.2 Scenario (ii): Collision Avoidance at Low Local Traction

The second scenario is aimed at replicating the conditions when a pedestrian has suddenly entered the lane from the side of the road. At the start of the second scenario, $t_c = 0$ s, the pedestrian has been detected by the vehicle's perception stack and the planner/controller starts reacting. The initial velocity of the vehicle is 8m/s and the pedestrian is detected 20m ahead of the vehicle. Traction conditions are the same as in the previous case, i.e., $\mu_{gt}(s) = 0.8$ for $s < 0$ and $\mu_{gt}(s) = 0.2$ for $s \geq 0$. The NA scheme operates under static tire force constraints corresponding to a static friction estimate of $\mu_{sta} = 0.8$, while the adaptive scheme sets its tire force constraints dynamically according to $\mu_{est}(s) = \mu_{gt}(s)$. The objective of the vehicle is to avoid collision with the obstacle, while minimizing deviations from the lane center. The performance of the NA and TA schemes in this scenario is presented in Fig. 5.

Not Adapting to Low Local Traction

Under the non-adaptive scheme, we make the following observations. Upon detecting the pedestrian, Fig. 5a, the NA scheme initiates an aggressive maneuver (i.e., high curvature given the speed) that is meant to quickly move the vehicle away from its collision course with the obstacle. However, the vehicle is not able to realize the aggressive motion, so the plan is gradually shifted forward ahead of the vehicle. At $t_c = 2$ s, Fig. 5c, the vehicle has eventually moved 2m to the right of the centerline, Fig. 5j, enough to clear the obstacle. However, this occurs closer to the obstacle than was planned at $t_c = 0$ s. Also, at this point the vehicle exhibits heavy under-steering behavior while turning right (see plotted front slip angle in Fig. 5l). After clearing the obstacle, the vehicle starts steering left to return back to the lane, but the grip is insufficient to counteract the motion out of the lane that was initiated during the first part of the maneuver. At $t_c = 3.1$ s, Fig. 5e, the high slip angles has lead to a complete loss of control authority, and the vehicle is veering out of the lane. At this point in the experiment, the planner disengages and full brake is activated. The vehicle eventually comes to a stop 7m outside of the lane Fig. 5g.

The underlying reason is again revealed by the planned tire forces at $t_c = 0$ s, plotted in Fig. 5i.

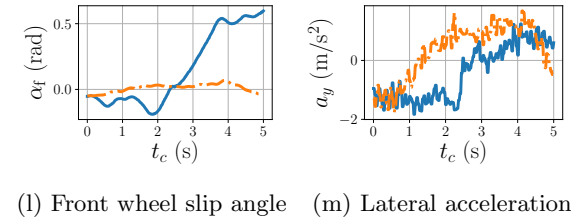
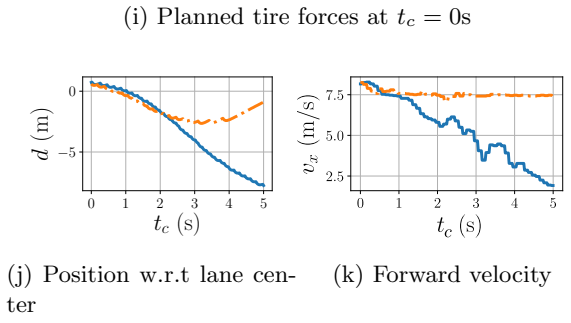
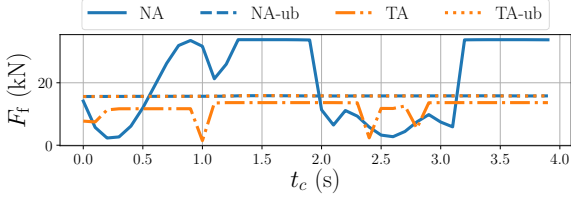
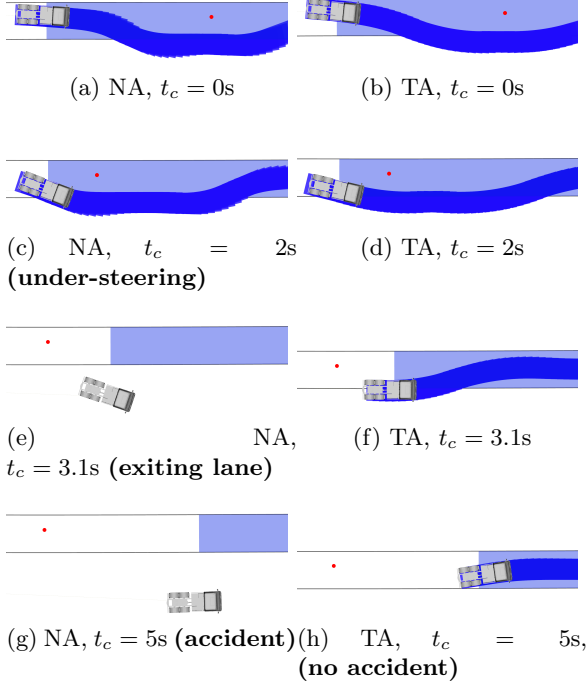


Figure 5: Scenario (ii), collision avoidance at Low traction conditions. Subfigures 5a through 5h show overhead visualizations of the planned motion. The left and right columns corresponds to the non-adaptive (NA) and traction adaptive (TA) schemes respectively. Subfigure 5i show planned tire forces and prevailing force limits for the front tire at $t_c = 0s$. Subfigures 5j, 5k, 5l and 5m show comparisons in terms of deviation from the lane center, forward velocity, front wheel slip angle and lateral acceleration.

The NA scheme (solid blue), plans tire forces that exceed the physical limit (dotted blue), and therefore, the planned motion is not physically attainable. The fact that the real vehicle cannot realize the planned motion has two separate unfavorable consequences in this case: First, the vehicle cannot change direction as fast as the planner dictates, therefore, the margin to the obstacle ends up being smaller than what was originally planned, see Figs. 5a and 5c. Second, the overly aggressive maneuver leads to high slip angles, Fig. 5l, which eventually leads to complete loss of control authority, Fig. 5e, due to tire saturation [5].

Adapting to Low Local Traction

As we saw in the previous scenario, the TA scheme dynamically updates tire force constraints such that the planned motions are dynamically feasible with respect to the local traction conditions. Therefore, in this case we observe that the initial plan from the TA scheme at $t_c = 0$ s, Fig. 5b is a less aggressive maneuver compared to the NA scheme. At $t_c = 2$ s, Fig. 5b, the vehicle has moved 2m to the right of the centerline, enough to clear the obstacle, without generating excessive front wheel slip Fig. 5l. At $t_c = 3.1$ s, Fig. 5f, the vehicle has cleared the obstacle and at $t_c = 5$ s, Fig. 5h, the vehicle is returning from a comparatively small deviation from the lane, maintaining full control authority.

Fig. 5i reveals that the planned motion from the TA scheme at $t_c = 0$ s exploits approximately 90% ($\lambda = 0.90$) of the available traction force for large parts of the maneuver (dash-dotted orange), while the NA scheme (solid blue) exceeds the traction bound by a large margin. Hence, apart from a small margin to the absolute traction limit, it delivers the most aggressive plan that is achievable within at the prevailing conditions, yielding manageable slip angles, Fig. 5l, and therefore maintained control authority. As such, the critical scenario is mitigated.

Furthermore, we observe from Fig. 5j, showing deviation from the lane center, that for the first two seconds of the evasive maneuver, the sideways motion of the vehicle is almost identical for the two schemes. From this we get an indication that sacrificing control authority of the vehicle in an overly aggressive maneuver, does not improve the capacity to avoid colliding with the obstacle. It does however increase the risk of a secondary accident as the vehicle enters the opposing lane at high speed in an uncontrolled manner.

6.3 Scenario (iii): Collision Avoidance at High Local Traction

A naive solution for handling scenarios 1 and 2 with static tire force constraints is to select a conservative static constraint, corresponding to the worst case traction. However, this strategy will restrict the utilization of the vehicle's capability at favorable traction conditions. Next, we investigate this aspect for collision avoidance at high μ .

In this scenario, $\mu_{gt}(s) = 0.8$ for $s \geq 0$, and the pedestrian is detected 15m ahead of the vehicle. The initial velocity of the vehicle is 15m/s. The NA scheme operates under static tire force constraints corresponding to a *conservative* static friction estimate of $\mu_{sta} = 0.4$, while the adaptive scheme sets its tire force constraints dynamically according to $\mu_{est}(s) = \mu_{gt}(s)$ as in previous scenarios. Performance for the NA and TA schemes in this scenario is presented in Fig. 6.

Not Adapting to High Local Traction

For the NA scheme, we make the following observations. Upon detecting the pedestrian, Fig. 6a, the planner initiates an evasive maneuver under conservative static tire force constraints. Given the vehicle state at the time when the planner/controller starts reacting to the obstacle, in combination with the restrictive tire force constraints, there is no collision free solution to the motion planning

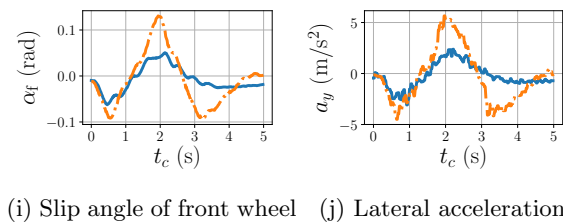
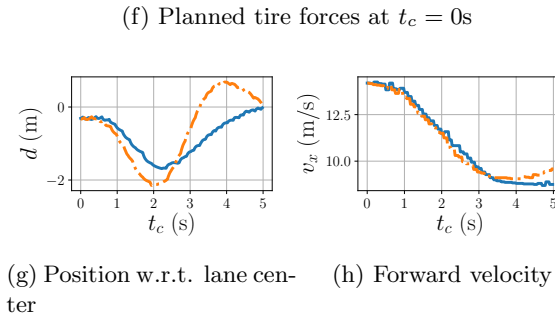
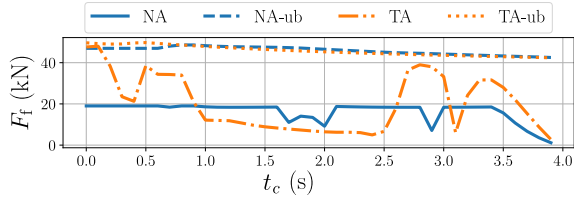
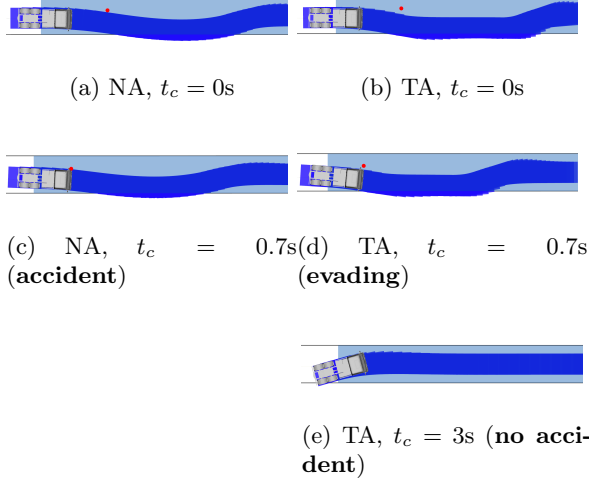


Figure 6: Scenario (iii), collision avoidance at high μ . Subfigures 6a through 6e show overhead visualizations of the vehicle position and the planned motion. The left and right columns of overhead views corresponds to the non-adaptive (NA) and traction adaptive (TA) schemes respectively. Subfigure 6f show planned tire forces and prevailing force limits for the front tire at $t_c = 0s$. Subfigures 6g, 6h, 6i and 6j show a comparison in terms of deviation from the lane center, forward velocity, front wheel slip angle and lateral acceleration.

problem. As a result, the planner selects the least violating trajectory. At $t_c = 0.7\text{s}$, Fig. 6c, the vehicle is colliding with the obstacle at a velocity of 13.9 m/s. Notice that in this scenario the final motion of the vehicle corresponds well with the initial plan from the NA scheme, which was not the case in the low μ scenario. This is because in this case, the NA scheme is not violating the physical limitations in terms of tire forces, see Fig. 6f (blue dots). Rather, traction force utilization for the front wheel is consistently below 50% throughout the maneuver.

Adapting to High Local Traction

Because $\mu_{\text{est}}(s) > \mu_{\text{sta}}$ in this case, adapting the tire force constraints means expanding the set of allowed tire forces compared to the NA case. Hence, the TA scheme is able to produce a more aggressive plan at $t_c = 0\text{s}$, Fig. 6b, that manages to avoid colliding with the obstacle. At $t_c = 0.7\text{s}$, Fig. 6d, the vehicle passes beside the obstacle as per the initial plan, and at $t_c = 3\text{s}$, Fig. 6e, the vehicle is returning to the lane, fully recovered from the incident. Fig. 6f reveals that at $t_c = 0\text{s}$, the TA scheme plans to exploit a larger part available traction. This is also reflected by the measured front slip angle, Fig. 6i.

Also, in this scenario, because of the higher accelerations, the effect of dynamic normal loads become more apparent, see Fig. 6f. In the beginning of the maneuver, when the vehicle is braking hard, the normal force, and hence the maximum horizontal force, is larger on the front tire and smaller on the rear. Notice that the TA scheme is able to exploit also this effect, and allocates 12% higher front tire force to the front tire at the start of the maneuver (while the vehicle is braking hard) compared to the end of the maneuver (when the vehicle is no longer decelerating). Although this effect is small compared to the 50% difference between the TA and NA schemes due to the friction estimate, it is not insignificant. The effect will be more pronounced at higher accelerations, and thus, is even more important to consider for vehicles that are smaller and more agile than our 8.5 ton test vehicle.

The higher utilization of the available traction for the TA scheme leads to a more rapid sideways motion compared to the NA scheme Fig. 6g, and for this case, such a performance difference represents the difference between success and failure of the collision avoidance maneuver. Here, in contrast to Scenarios (i) and (ii), the TA scheme mitigates the critical situation by *expanding* the tire force constraints instead of reducing them. In all three cases however, it utilizes around 90% of the locally available traction.

From this example we conclude that conservative friction estimation may reduce collision avoidance performance. To further investigate the extent of this phenomenon, we ran three configurations of the planning/ctrl schemes, TA with $\mu_{\text{est}} = 0.8$, NA with $\mu_{\text{sta}} = 0.6$ and NA with $\mu_{\text{sta}} = 0.4$, through a sequence of 40 challenging collision avoidance scenarios each. A sequence of relative positions of the suddenly appearing obstacles was pre-generated by sampling from a uniform distribution, $-1.0\text{m} \leq d_{\text{obs}} \leq 1.0\text{m}$, $s + 11.0\text{m} \leq s_{\text{obs}} \leq s + 13.0\text{m}$. The initial velocity at obstacle detection was 10m/s.

With the three configurations, the vehicle managed to avoid collision in 11/40, 6/40 and 4/40 cases, respectively. Fig. 7 shows individual differences in terms of minimum distance margin to the obstacle, Δ_m , for the 11 cases in which at least one configuration performed a successful avoidance maneuver.

Note that the most conservative configuration (NA with $\mu_{\text{sta}} = 0.4$), has the least amount of successful avoidance maneuvers, and the four successful avoidance maneuvers are very near misses, with less than 0.10m of clearance to the obstacle. The least conservative configuration (TA with $\mu_{\text{est}} = 0.8$) has the largest number of successful avoidance maneuvers and tends to also have the largest amount of clearance to the avoided obstacles. This is true for all cases except for obstacles 5

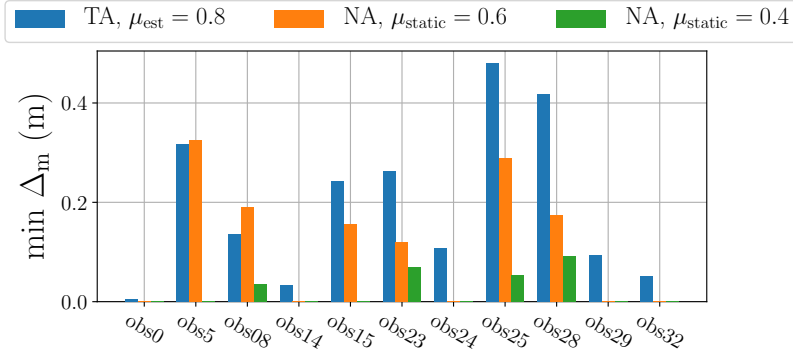


Figure 7: Minimum distances to avoided obstacles for three configurations of the planner: traction adaptive (TA) with $\mu_{\text{est}} = 0.8$ (blue), non-adaptive (NA) with static tire force constraints corresponding to $\mu_{\text{sta}} = 0.6$ (orange), non-adaptive (NA) with static tire force constraints corresponding to $\mu_{\text{sta}} = 0.4$ (green). Zero value corresponds to collision.

and 8, where (NA with $\mu_{\text{sta}} = 0.6$) has slightly higher margin. We believe this stems from variations in the state of the vehicle when the obstacle is detected. In particular, the lateral position within the lane exhibited small variations during the experiment, which had noticeable effect on the margin to the obstacle.

6.4 Scenario (iv): Collision Avoidance with Discrete Decisions

As mentioned in Section 4.4, the RTI method handles situations when the initial guess $\hat{\mathcal{T}}_t$ violates state constraints, $\hat{x}_{k|t} \notin \mathcal{P}_{k|t}^{\mathcal{X}}$, for any $k \in \{0, 1, \dots, N\}$, by softening the constraints and giving constraint violations a high cost. This in combination with the fact that the algorithm only searches for a solution locally around $\hat{\mathcal{T}}_t$ leads to sensitivity to highly suboptimal local minima. The problem occurs when the constraint configuration changes abruptly between planning iterations e.g., at suddenly appearing obstacles, or in our approach to traction adaptation, at large changes in traction conditions. Therefore, we employ the sampling augmentation procedure, see Sections 5.2 and 5.3, to mitigate this problem. In this section we evaluate the safety implications of sampling augmentation in critical scenarios with discrete decisions.

Scenario (iv) is a collision avoidance scenario where two obstacles appear simultaneously 20m and 35m in front of the vehicle. The first obstacle appears on the left side of the lane and the second on the right side of the lane. State constraints are set when such that obstacles should be avoided by a margin of 0.5m. We compare performance of the non-augmented RTI scheme (abbreviated RTI), with our sampling augmented variant (abbreviated SA). For this test both schemes use the same static tire force constraints. Results are presented in Fig. 8.

Without Sampling Augmentation (RTI)

When the obstacles are detected at $t_c = 1.0\text{s}$, Fig 8a, the non-augmented RTI scheme produces an evasive plan that avoids the obstacles by going in between them (right of the first and left of the second obstacle). The vehicle manages to avoid collision, Figs. 8c, 8e, but needs to use the maximum front tire force almost throughout the maneuver, Fig. 8g, and has a very small distance margin Δ_m to the obstacles (state constraints are violated), Fig. 8j.

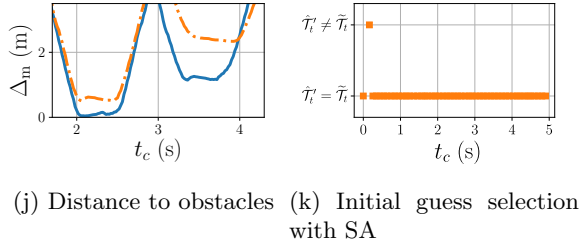
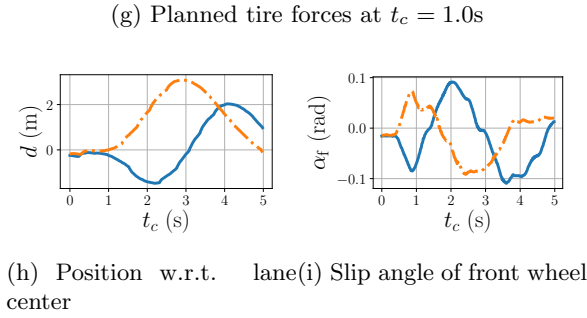
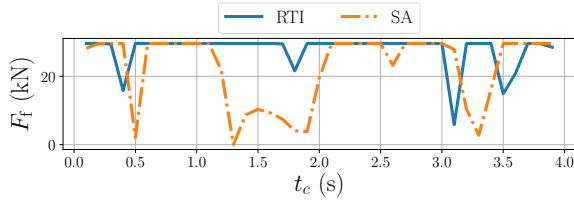
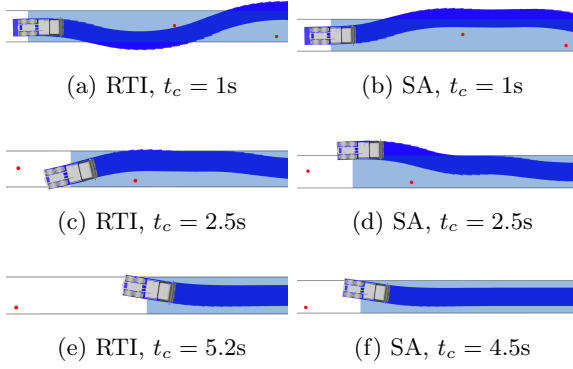


Figure 8: Scenario (iv), collision with discrete decisions. Subfigures 8a through 8f show overhead visualizations of the vehicle position and the planned motion. The left and right columns of overhead views correspond to the non-augmented RTI scheme (RTI) and sampling augmented (SA) schemes respectively. Subfigure 8g show planned tire forces for the front tires at $t_c = 1.0s$. Subfigures 8h, 8i and 8j show a comparison in terms of deviation from the lane center, front wheel slip angle and smallest distance to either obstacle. Subfigure 8k shows which candidate was selected as initial guess with the SA scheme.

The decision to plan the maneuver between the obstacles stems from the last planning iteration before the obstacles appeared. At the first planning iteration after the obstacle is detected, the solution from the previous iteration \mathcal{T}_{t-1}^* and hence the initial guess, $\hat{\mathcal{T}}_t$, is at the center of the lane. When the obstacles appear, $\hat{\mathcal{T}}_t$ violates the state constraints, $\hat{x}_{k|t} \notin \mathcal{P}_{k|t}^{\mathcal{X}}$ for some $k \in \{0, 1, \dots, N\}$. Since state constraints are soft, the optimization problem is still feasible, but the decision of adjusting the trajectory left or right of an obstacle is determined by minimizing cost locally around \mathcal{T}_{t-1}^* , resulting in a decision to go between the obstacles.

With Sampling Augmentation (SA)

When the sampling augmented RTI algorithm is exposed to the same scenario, we observe that upon detecting the obstacle, the SA scheme produces an evasive plan to the left of both obstacles instead, Fig. 8b. When following this plan, the vehicle is able to clear the obstacles more comfortably, Figs. 8c, 8e. It uses the maximum front tire force a smaller amount of the time, Fig. 8g, keeps above the minimum margin to both obstacles (not violating state constraints), Fig. 8j and recovers more quickly after the incident (compare Fig. 8e and Fig. 8f).

Just as before, at the first planning iteration after the obstacles are detected, the initial guess $\tilde{\mathcal{T}}_t$ originating from \mathcal{T}_{t-1}^* is in collision with the obstacles. However, due to the sampling augmentation procedure, at $t_c = 0.1s$, a sampled trajectory $\hat{\mathcal{T}}'_t$ is selected as initial guess. In the subsequent planning iterations throughout the maneuver, $\tilde{\mathcal{T}}_t$ is selected, Fig. 8k.

Fig. 8k reveals that the sampled trajectories were only used in a single planning iteration just after the obstacles appeared. This indicates that sampling augmentation steps in exactly when it needs to avoid unfavorable local minima, i.e., at rapid changes in the constraint configuration of the motion planning problem. Otherwise, when changes to the constraint configuration are small, $\tilde{\mathcal{T}}_t$ typically has the lowest cost and gets selected. This result indicates that sampling augmentation alleviates the drawbacks of RTI, without impairing its otherwise desirable properties described in [16].

Because the sampled trajectories, are spread throughout the physically reachable drivable area, the decision to go left, right or in between the obstacles is not solely determined by local information around \mathcal{T}_{t-1}^* as in the non-augmented case, but over a wide range of feasible maneuvers of the vehicle, represented by $\hat{\mathcal{S}}_t \cup \tilde{\mathcal{T}}_t$. This result shows that the steps taken for sampling augmentation (A-D of Section 4), effectively mitigates the drawbacks of RTI (see Section 4.4) with respect to our problem formulation.

7 Conclusions and Future Work

In this paper we address the problem of motion planning at the limits of handling under locally varying traction conditions. We evaluate the proposed traction adaptive algorithm by comparing it to an equivalent non-adaptive scheme in a sequence of critical scenarios at various traction conditions. Results from experimental evaluation indicate that traction adaptation improves capacity to avoid accident in all four tested critical scenarios. The proposed algorithm's performance in this regards stems from two properties:

1. Ensured dynamic feasibility of planned motions, even at poor local traction conditions.
2. A high ratio (90% for the tested configuration) of locally available traction is utilized to avoid collision if necessary.

Moreover, we experimentally demonstrate that the sampling augmentation procedures (steps A-D of Section 5) of the proposed algorithm successfully mitigates the computational challenges associated with infeasibility and sensitivity to local minima (listed in Section 4.4) that emerges in the planning problem at rapid changes to the constraint configuration.

In this study, friction estimation has been replaced by preparatory measurements at the test track. Consideration of estimation uncertainty, and incorporating an integrated road friction estimation framework with control design are left for future research.

Acknowledgment

The authors gratefully acknowledge the AutoDrive project, H2020-ECSEL, SAFER Open Research at AstaZero and Integrated Transport Research Lab at KTH for financial support. Furthermore we would like to thank Fredrik von Corswant, Henrik Biswanger as well as the staff at the AstaZero and Stora Holm test tracks for their support with the experiments.

References

- [1] Philip Koopman, Beth Osyk, and Jack Weast. Autonomous vehicles meet the physical world: Rss, variability, uncertainty, and proving safety. In Alexander Romanovsky, Elena Troubitsyna, and Friedemann Bitsch, editors, *Computer Safety, Reliability, and Security*, pages 245–253, Cham, 2019. Springer International Publishing.
- [2] Alexander Liniger, Alexander Domahidi, and Manfred Morari. Optimization-based autonomous racing of 1: 43 scale rc cars. *Optimal Control Applications and Methods*, 36(5):628–647, 2015.
- [3] J. K. Subosits and J. C. Gerdes. From the racetrack to the road: Real-time trajectory replanning for autonomous driving. *IEEE Transactions on Intelligent Vehicles*, 4(2):309–320, June 2019.
- [4] DB Fambro, K Fitzpatrick, and RJ Koppa. Nchrp report 400: Determination of stopping sight distances. *TRB, National Research Council, Washington, DC*, 1997.
- [5] Rajesh Rajamani. *Vehicle dynamics and control*. Springer Science & Business Media, 2011.
- [6] John P Alsterda, Matthew Brown, and J Christian Gerdes. Contingency model predictive control for automated vehicles. *arXiv preprint arXiv:1903.08818*, 2019.
- [7] L. Svensson, M. Bujarbaruah, N. R. Kapania, and M. Törngren. Adaptive trajectory planning and optimization at limits of handling. In *2019 IEEE/RSJ International Conference on Intelligent Robots and Systems (IROS)*, pages 3942–3948, 2019.
- [8] Brian Paden, Michal Čáp, Sze Zheng Yong, Dmitry Yershov, and Emilio Frazzoli. A survey of motion planning and control techniques for self-driving urban vehicles. *IEEE Transactions on intelligent vehicles*, 1(1):33–55, 2016.
- [9] David González, Joshué Pérez, Vicente Milanés, and Fawzi Nashashibi. A review of motion planning techniques for automated vehicles. *IEEE Trans. Intelligent Transportation Systems*, 17:1135–1145, 2016.

- [10] Julius Ziegler, Philipp Bender, Thao Dang, and Christoph Stiller. Trajectory planning for bertha—a local, continuous method. In *Intelligent Vehicles Symposium Proceedings, 2014 IEEE*, pages 450–457. IEEE, 2014.
- [11] Stephen Boyd and Lieven Vandenbergh. *Convex optimization*. Cambridge university press, 2004.
- [12] John T Betts. Survey of numerical methods for trajectory optimization. *Journal of guidance, control, and dynamics*, 21(2):193–207, 1998.
- [13] Charles R Hargraves and Stephen W Paris. Direct trajectory optimization using nonlinear programming and collocation. *Journal of Guidance, Control, and Dynamics*, 10(4):338–342, 1987.
- [14] Oskar Von Stryk and Roland Bulirsch. Direct and indirect methods for trajectory optimization. *Annals of operations research*, 37(1):357–373, 1992.
- [15] Moritz Diehl, H Georg Bock, Johannes P Schlöder, Rolf Findeisen, Zoltan Nagy, and Frank Allgöwer. Real-time optimization and nonlinear model predictive control of processes governed by differential-algebraic equations. *Journal of Process Control*, 12(4):577–585, 2002.
- [16] Moritz Diehl, Hans Georg Bock, and Johannes P Schlöder. A real-time iteration scheme for nonlinear optimization in optimal feedback control. *SIAM Journal on control and optimization*, 43(5):1714–1736, 2005.
- [17] Moritz Diehl, Rolf Findeisen, Frank Allgöwer, Hans Georg Bock, and Johannes P Schlöder. Nominal stability of real-time iteration scheme for nonlinear model predictive control. *IEE Proceedings-Control Theory and Applications*, 152(3):296–308, 2005.
- [18] M. Werling and D. Liccardo. Automatic collision avoidance using model-predictive online optimization. In *2012 IEEE 51st IEEE Conference on Decision and Control (CDC)*, pages 6309–6314, Dec 2012.
- [19] Ivo Batkovic, Mario Zanon, Mohammad Ali, and Paolo Falcone. Real-time constrained trajectory planning and vehicle control for proactive autonomous driving with road users. *arXiv preprint arXiv:1903.07743*, 2019.
- [20] Thomas M Howard, Colin J Green, Alonzo Kelly, and Dave Ferguson. State space sampling of feasible motions for high-performance mobile robot navigation in complex environments. *Journal of Field Robotics*, 25(6-7):325–345, 2008.
- [21] Dave Ferguson, Thomas M. Howard, and Maxim Likhachev. Motion planning in urban environments. *Journal of Field Robotics*, 25(11-12):939–960, 2008.
- [22] Moritz Werling, Sören Kammel, Julius Ziegler, and Lutz Gröll. Optimal trajectories for time-critical street scenarios using discretized terminal manifolds. *The International Journal of Robotics Research*, 31(3):346–359, 2012.
- [23] Fredrik Gustafsson. Slip-based tire-road friction estimation. *Automatica*, 33(6):1087–1099, 1997.
- [24] Rajesh Rajamani, Gridsada Phanomchoeng, Damrongrit Piyabongkarn, and Jae Y Lew. Algorithms for real-time estimation of individual wheel tire-road friction coefficients. *IEEE/ASME Transactions on Mechatronics*, 17(6):1183–1195, 2012.

- [25] J. Yi, L. Alvarez, and R. Horowitz. Adaptive emergency braking control with underestimation of friction coefficient. *IEEE Transactions on Control Systems Technology*, 10(3):381–392, May 2002.
- [26] Luis Alvarez, Jingang Yi, Roberto Horowitz, and Luis Olmos. Adaptive emergency braking control with observer-based dynamic tire/road friction model and underestimation of friction coefficient. *IFAC Proceedings Volumes*, 35(1):211–216, 2002.
- [27] P. Falcone, F. Borrelli, J. Asgari, H. E. Tseng, and D. Hrovat. Predictive active steering control for autonomous vehicle systems. *IEEE Transactions on Control Systems Technology*, 15(3):566–580, May 2007.
- [28] Yiqi Gao, Theresa Lin, Francesco Borrelli, Eric Tseng, and Davor Hrovat. Predictive control of autonomous ground vehicles with obstacle avoidance on slippery roads. In *Dynamic systems and control conference*, volume 44175, pages 265–272, 2010.
- [29] S. Roychowdhury, M. Zhao, A. Wallin, N. Ohlsson, and M. Jonasson. Machine learning models for road surface and friction estimation using front-camera images. In *2018 International Joint Conference on Neural Networks (IJCNN)*, pages 1–8, July 2018.
- [30] M. Nolte, N. Kister, and M. Maurer. Assessment of deep convolutional neural networks for road surface classification. In *2018 21st International Conference on Intelligent Transportation Systems (ITSC)*, pages 381–386, Nov 2018.
- [31] F. Holzmann, M. Bellino, R. Siegwart, and H. Bubb. Predictive estimation of the road-tire friction coefficient. In *2006 IEEE Conference on Computer Aided Control System Design*, pages 885–890, Oct 2006.
- [32] R. Omer and L. Fu. An automatic image recognition system for winter road surface condition classification. In *13th International IEEE Conference on Intelligent Transportation Systems*, pages 1375–1379, Sep. 2010.
- [33] Y. Qian, E. J. Almazan, and J. H. Elder. Evaluating features and classifiers for road weather condition analysis. In *2016 IEEE International Conference on Image Processing (ICIP)*, pages 4403–4407, Sep. 2016.
- [34] Marko Tanaskovic, Lorenzo Fagiano, Roy Smith, and Manfred Morari. Adaptive receding horizon control for constrained mimo systems. *Automatica*, 50(12):3019–3029, 2014.
- [35] L. Hewing, J. Kabzan, and M. N. Zeilinger. Cautious model predictive control using gaussian process regression. *IEEE Transactions on Control Systems Technology*, pages 1–8, 2019.
- [36] Johannes Köhler, Elisa Andina, Raffaele Soloperto, Matthias A Müller, and Frank Allgöwer. Linear robust adaptive model predictive control: Computational complexity and conservatism. In *Conference on Decision and Control (CDC)*, pages 1383–1388. IEEE, 2019.
- [37] Lukas Hewing, Kim P Wabersich, Marcel Menner, and Melanie N Zeilinger. Learning-based model predictive control: Toward safe learning in control. *Annual Review of Control, Robotics, and Autonomous Systems*, 3:269–296, 2020.
- [38] Luigi Chisci, J Anthony Rossiter, and Giovanni Zappa. Systems with persistent disturbances: predictive control with restricted constraints. *Automatica*, 37(7):1019–1028, 2001.

- [39] Wilbur Langson, Ioannis Chrysochoos, SV Raković, and David Q Mayne. Robust model predictive control using tubes. *Automatica*, 40(1):125–133, 2004.
- [40] Sébastien Gros, Mario Zanon, Rien Quirynen, Alberto Bemporad, and Moritz Diehl. From linear to nonlinear MPC: bridging the gap via the real-time iteration. *International Journal of Control*, pages 1–19, 2016.
- [41] B. Houska, H.J. Ferreau, and M. Diehl. An Auto-Generated Real-Time Iteration Algorithm for Nonlinear MPC in the Microsecond Range. *Automatica*, 47(10):2279–2285, 2011.
- [42] Eric C. Kerrigan and Jan M. Maciejowski. Soft constraints and exact penalty functions in model predictive control. In *Proc. UKACC International Conference on Control*, 2000.
- [43] Alain Micaelli and Claude Samson. *Trajectory tracking for unicycle-type and two-steering-wheels mobile robots*. PhD thesis, INRIA, 1993.
- [44] Hans B Pacejka and Egbert Bakker. The magic formula tyre model. *Vehicle system dynamics*, 21(S1):1–18, 1992.

Appendix A Experimental Setup

The vehicle used for the experiments was a Volvo FH16 6x4, a 750 hp tractor equipped with Volvo Dynamic Steering and I-Shift transmission, housed at the vehicle research laboratory *Resource for Vehicle Research* (REVERE) at Chalmers University of Technology. Table 1 outlines physical parameters of the vehicle. The truck is equipped with multiple sensors to perceive the vehicle’s state and surroundings such as a Velodyne VLP32C Ultra Puck lidar, a stereo vision system, a monocular camera system and an OxTS GPS/IMU unit that provides localization information and inertial data.



Figure 9: Volvo FH16 Tractor from Chalmers University of Technology at the Stora Holm low μ test track.

Furthermore, the truck is equipped with an embedded computing unit realized with an AAEON AEC-6950 that allows interfacing with the truck’s CAN network, i.e., to read CAN signals describing the vehicle state and to send actuation requests. This computer is also used to interface with the sensor stack. The computing system includes the microservices-based software stack OpenDLV⁴ that enables transparent communication of distributed software components using inter-process

⁴Cf. <https://github.com/chalmers-revere/opendlv>

Parameter	Value
m	8350 kg
I_z	8150 kgm ²
h	1.0 m
l_f	1.20 m
l_r	2.20 m

Table 1: Static physical parameters of test vehicle

communication (IPC), for example network communication and shared memory for low latency in real-time setups and for large volume sensor data handling.

The planning/control algorithms were integrated in a ROS stack of rudimentary autonomous functionality (localization, state estimation, track and object handling etc.) which was run on a PC with an Intel Core i7-7820HK CPU @ 2.9GHz and an Nvidia GeForce GTX 1070 GPU. On the truck's computing node, a ROS-to-OpenDLV bridge was realized for the project to enable access of the truck's actuators to the planning/control algorithms. Experiments were primarily conducted at the High Speed Area of the AstaZero test facility in Borås, Sweden, with complementary low μ tests at the Stora Holm test track in Gothenburg, Sweden.

Appendix B Dynamic Bicycle Model with Time-varying Tire Force Limits in Road Aligned Coordinates

We derive a dynamic bicycle model based on standard vehicle dynamics literature [5]. See Fig. 10 for the geometric relations of the model. From Newton's second law for the lateral dimension we have that

$$\dot{v}_y = \frac{1}{m}(F_{yf} + F_{yr}) - v_x\dot{\psi} + g \sin \phi,$$

where F_{yf} and F_{yr} are lateral forces on the front and rear tires respectively. The term $v_x\dot{\psi}$ is the centripetal acceleration and $g \sin \phi$ is the contribution from the bank angle of the road. As for the

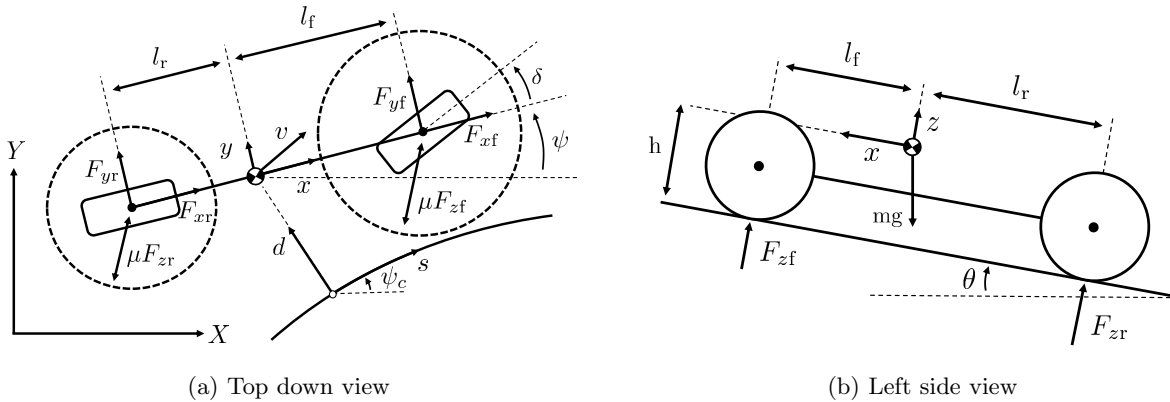


Figure 10: Geometric relations of the dynamic bicycle model with time-varying tire force limits in a road aligned coordinate frame.

longitudinal dynamics, we have that

$$\dot{v}_x = \frac{1}{m}(F_{xf} + F_{xr}) - g \sin(\theta),$$

where F_{xf} and F_{xr} are the controlled tractive forces on the front and rear tires respectively. The term $g \sin(\theta)$ represent the longitudinal acceleration contribution due to the inclination of the road.

The yaw dynamics are given by moment balance around the z -axis as

$$\ddot{\psi} = \frac{1}{I_z} (l_f F_{yf} - l_r F_{yr}),$$

where I_z is the vehicle's moment of inertia about the z -axis, and l_f and l_r are the distances from the center of mass to the front and rear axle respectively.

In order to capture the motion of the vehicle relative to the road we use a road aligned coordinate frame [43]. A coordinate s represents the progress along the centerline of the lane and a coordinate d represents the lateral deviation from the centerline, as depicted in Fig. 10a. The d -coordinate increases to the left. Variables ψ_c κ_c denote the path tangent, and path curvature at the point on the centerline, where the vehicle position is perpendicular to the centerline tangent. $\Delta\psi = \psi - \psi_c$ represents the relative angle between the vehicle yaw angle and the tangent of the centerline. Geometric relations of the coordinate system definition give us the evolution of s , d and $\Delta\psi$. Finally we express the continuous time dynamics as

$$\begin{aligned} \dot{s} &= \frac{v_x \cos(\Delta\psi) - v_y \sin(\Delta\psi)}{1 - d\kappa_c}, \\ \dot{d} &= v_x \sin(\Delta\psi) + v_y \cos(\Delta\psi), \\ \Delta\dot{\psi} &= \dot{\psi} - \kappa_c \frac{v_x \cos(\Delta\psi) - v_y \sin(\Delta\psi)}{1 - d\kappa_c}, \\ \ddot{\psi} &= \frac{1}{I_z} (l_f F_{yf} - l_r F_{yr}), \\ \dot{v}_x &= \frac{1}{m} (F_{xf} + F_{xr}) - g \sin(\theta), \\ \dot{v}_y &= \frac{1}{m} (F_{yf} + F_{yr}) - v_x \dot{\psi} + g \sin \phi. \end{aligned} \quad (14)$$

By selecting the state and control vectors as $x = [s, d, \Delta\psi, \dot{\psi}, v_x, v_y]^\top$ and $u = [F_{yf}, F_{xf}, F_{xr}]^\top$ we can compactly write the planning model (14) as $\dot{x} = f_p(x, u)$.

The rear lateral force F_{yr} is not included among the control inputs, instead it is computed from the state through a time-varying linear tire model

$$F_{yr} = \tilde{C}_r(\mu) \alpha_r \quad (15)$$

with the rear slip angle $\alpha_r = -\arctan((v_y - l_r \dot{\psi})/v_x)$. The time-varying rear cornering stiffness \tilde{C}_r is obtained by linearizing Pacejka's Magic Formula tire model, [44],

$$\begin{aligned} F_y &= D(\mu) \sin(C(\mu) \arctan(B(\mu) \alpha_f + \dots \\ &\quad - E(\mu) (B(\mu) \alpha_f - \arctan(B(\mu) \alpha_f)))), \end{aligned}$$

with parameters $B(\mu)$, $C(\mu)$, $D(\mu)$ and $E(\mu)$ obtained as functions of μ from a look-up table that approximately associate the tire parameters to the friction coefficient for various road surface

conditions. Further motivation of the choice of a linear time-varying linear tire model is provided at the end of this appendix.

The normal forces F_{zf} and F_{zr} acting on the tires of the model are obtained from moment balances about the contact points of the rear and front tires respectively as

$$\begin{aligned} F_{zf} &= \frac{1}{l_f + l_r} (-m\dot{v}_x h - mgh \sin \theta + mgl_r \cos \theta), \\ F_{zr} &= \frac{1}{l_f + l_r} (m\dot{v}_x h + mgh \sin \theta + mgl_f \cos \theta). \end{aligned} \quad (16)$$

See geometric relations in Fig 10b. Combining these relations with the friction estimate μ we define front and rear *time-varying*⁵ force boundaries as

$$\begin{aligned} F_f^{(\text{ub})} &= \lambda \mu F_{zf}, \\ F_r^{(\text{ub})} &= \lambda \mu F_{zr} \end{aligned}$$

where $\lambda \in [0, 1]$ is a user adjustable traction utilization factor. If $\lambda = 1$, the algorithm is allowed to utilize the full friction circle. To comply with these bounds, tire force commands need to fulfill

$$\begin{aligned} F_{xf}^2 + F_{yf}^2 &\leq F_f^{(\text{ub})}, \\ -\sqrt{\left(F_r^{(\text{ub})}\right)^2 - (F_{yr})^2} &\leq F_{xr} \leq \sqrt{\left(F_r^{(\text{ub})}\right)^2 - (F_{yr})^2}. \end{aligned} \quad (17)$$

Remark 4 *In general, the linear tire model used in (15) does not accurately predict the relation between slip angle and tire force at high slip angles [5]. However, in this context, the combined lateral and longitudinal force command is always inside the friction circle, by a margin determined by the utilization factor λ . Inside such a boundary, a time-varying linear model corresponds well with the Magic Formula, see Fig. 11. Considering the computational trade-off mentioned in Section 2, this design represents a compromise between complexity and accuracy that have proven to be practically viable for our application.*

In addition to the bounded tire forces (17), the drivetrain of the vehicle imposes additional constraints

$$\begin{aligned} F_{xf} &\leq 0, \\ F_{xr} &\leq F_r^{(\text{ub}, \text{dr})}, \end{aligned} \quad (18)$$

due to rear wheel drive and limited tractive force from the motor $F_r^{(\text{ub}, \text{dr})}$.

Finally, the algorithmic framework used in this paper requires linear input constraints. To accommodate this, we under-approximate the input constraints (17) and (18) (for any prediction step k) by a three-dimensional polytope $\mathcal{P}^{\mathcal{U}}$, visualized in Fig. 12.

Appendix C Low-Level Control Interface

The vehicle model described in Appendix B is formulated with tire force control inputs rather than the control inputs of the actual test vehicle, i.e., steering angle request δ_{req} and acceleration request

⁵ Variables μ , F_{zf} and F_{zr} vary in time and hence, so does $F_f^{(\text{ub})}$ and $F_r^{(\text{ub})}$. Just as with the state variables in (14) the time dependency is omitted from the equations to simplify notation.

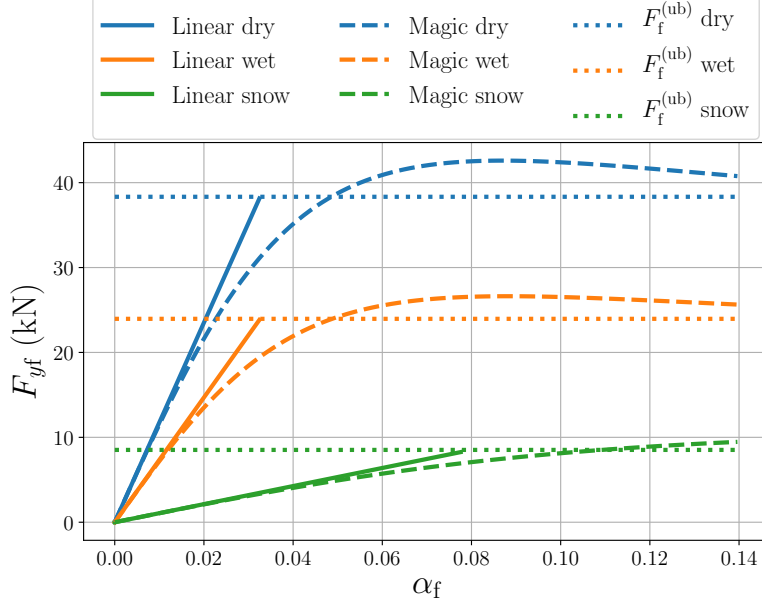


Figure 11: Comparison between nonlinear and linearized Magic Formula curves for different road surface conditions in relation to our force boundary at $\lambda = 0.9$.

a_{req} . Therefore, an additional procedure is required to translate tire force commands, F_{yf} , F_{xf} and F_{xr} to δ_{req} and a_{req} . For the longitudinal control input, the transformation is trivially computed as

$$a_{\text{req}} = (F_{xf} + F_{xr})/m.$$

For the steering input δ_{req} , we begin by computing the kinematic component of the steering angle, given by δ_{kin} , i.e., the steering angle that would yield the planned motion in the absence of tire slip. We fit a circle segment of curvature ρ to the Cartesian position representation of states $s_{k|t}^*$ and $d_{k|t}^*$ for $k \in \{0, 1, \dots, (N_{\text{fit}})\}$ of \mathcal{T}_t^* , where N_{fit} is tuned to get a representable fit. Then, the kinematic steering angle component is obtained as:

$$\delta_{\text{kin}} = \rho(l_f + l_r).$$

The dynamic steering angle component, i.e., the desired front wheel slip angle α_f , is obtained as

$$\alpha_f = F_{yf}/\tilde{C}_f,$$

where the time-varying cornering stiffness \tilde{C}_f is obtained by linearizing the Pacejka Magic Formula tire model as per the procedure described in Appendix B. The steering angle request is then obtained as

$$\delta_{\text{req}} = \delta_{\text{kin}} + \alpha_f,$$

Finally, the control commands δ_{req} and a_{req} are passed to the vehicle via the ROS-to-OpenDLV bridge described in Appendix A.

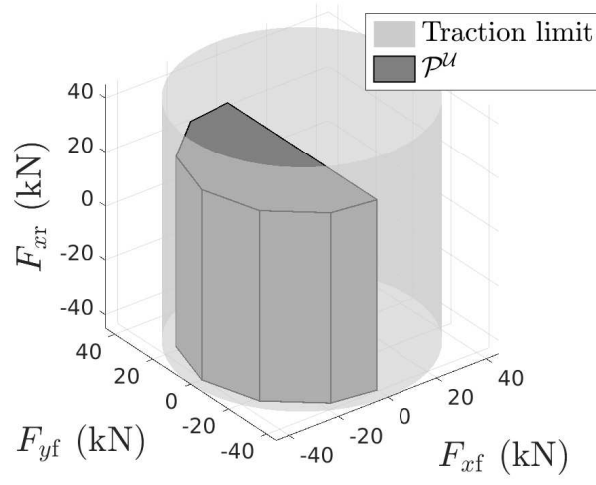


Figure 12: Input constraint polytope \mathcal{P}^u (for any prediction step) bounding control signals produced by the algorithm (dark gray) and theoretical traction limits according to (1).